COMPARISON OF LIGHTHILL'S ANALOGY AND ACOUSTIC PERTURBATION EQUATIONS FOR THE PREDICTION OF HVAC BLOWER NOISE

Matthias TAUTZ[1], Manfred KALTENBACHER[2], Stefan BECKER[1]

[1] *FAU, Institute of Process Machinery and Systems Engineering, Cauerstraße 4, 91058 Erlangen, Germany*

[2] *TU Vienna, Institute of Mechanics and Mechatronics, Getreidemarkt 9/325, 1060 Vienna, Austria*

SUMMARY

In this study, the analogy of Lighthill and the acoustic perturbation equations are compared regarding their usability on radial blower noise. First of all, flow simulations are performed by use of a commercial finite volume solver. Subsequently, aeroacoustic sources are computed and after their interpolation to a finite element grid the acoustic propagation to microphones is simulated. The influence of the used acoustic source region, CFD mesh size and CAA mesh size on spectra obtained in the far-field are investigated. In comparison to experimental results a good agreement could be achieved for both aeroacoustic approaches.

INTRODUCTION

The prediction of noise emitted from rotating turbomachineries is a major concern in many industries. Products that directly affect the comfort of costumers are of particular interest. In this context, our aim is to develop reliable tools for the aeroacoustic noise simulation of radial blowers in heating, ventilation and air conditioning (HVAC) systems. Therefore we used a hybrid, volume discretized approach. At its first step, the flow field was computed by application of the commercial finite volume solver Star-CCM+, where the WALE large eddy simulation (LES) turbulence model was used and constant density was assumed, which reduced the computational cost to receive a non-stationary flow field. As a consequence, no acoustic information was incorporated in the flow pressure. In the second step, aeroacoustic sources were evaluated on the flow mesh and conservatively interpolated onto a coarse finite element mesh, that was used used in the final step by the in-house code CFS++ [1] to evaluate the sound propagation by using non-homogeneous wave equations. This simulation procedure is rather complex because two volume discrete meshes need to be created, which are furthermore split into a stationary and a rotating domain. Its major advantage is the full insight into the acoustic source distribution and propagation fields. The acoustic perturbation equations (APE) were used in form of

the perturbed convective wave equation (PCWE) and compared to Lighthill's analogy. The optimal simulation configuration was determined for each method by variation of the CFD mesh size, CAA mesh size and the spatial extent of the recognized sources.

GOVERNING EQUATIONS

For the solution of the flow field the incompressible Navier-Stokes equations were utilized, which is a standard feature of common flow solvers and therefore is discussed here. The sources of the acoustic analogy of Lighthill depend on the flow velocity $\boldsymbol{v}$. In the case of rotating parts, the simulation domain is typically split up into a rotating and a stationary part, which are separated by an interface which allows mass and momentum transport. In the rotating domain, it is appropriate to define the velocity in the reference frame of rotation $\boldsymbol{v}^r$ by Eq. (1), where $\boldsymbol{v}^s$ denotes the velocity of the solid parts in the rotating domain or the rigid body motion.

$$\boldsymbol{v}^r = \boldsymbol{v} - \boldsymbol{v}^s \tag{1}$$

At this point we also introduce the substantial derivative operator $\mathrm{D}/\mathrm{D}t$ defined by Eq. (2). The vector $\boldsymbol{v}_c$ is the convective velocity, which was set in dependence of the application and domain of this operator.

$$\frac{\mathrm{D}}{\mathrm{D}t} = \frac{\partial}{\partial t} + \boldsymbol{v}_c \frac{\partial}{\partial x} \tag{2}$$

The formulation of Lighthill's analogy [2, 3] used in this study is written as Eq. (3), where $\boldsymbol{T}$ is the symmetric Lighthill tensor and p' the pressure fluctuations, respectively.

$$\frac{1}{c_0^2}\frac{\mathrm{D}p'}{\mathrm{D}t} - \frac{\partial^2 p'}{\partial x^2} = \frac{\partial^2 \boldsymbol{T}}{\partial x^2} \tag{3}$$

Therefore, the assumption of isentropic sound propagation $\rho' c_0^2 = p'$ was used to derive an equation in terms of p' instead of the fluctuation density ρ'. The fluctuations p' are a superposition of the hydrodynamic p^h and the acoustic fluctuations p^a in the acoustic source region, whereas only p^a remained in the far-field. In contrast to the formula given by Lighthill himself, this formulations also contains the substantial derivative, whereby in the stationary domain $\boldsymbol{v}_c = 0$ was applied in order to regain the original wave operator used for the quiescent medium. In contrast, for the rotating region $\boldsymbol{v}_c = -\boldsymbol{v}^s$ was used to regain the assumption of the quiescent medium despite the grid movement. For the computation of the right-hand side the tensor $\boldsymbol{T}$ according to Eq. (4) was used inside stationary domain, where the operator $\otimes$ denotes the dyadic product and the overline the temporal average, respectively, which was subtracted because sources constant in time and space do not radiate any sound.

$$\boldsymbol{T} = b_s b_I \rho_0 \left(\boldsymbol{v} \otimes \boldsymbol{v} - \overline{\boldsymbol{v} \otimes \boldsymbol{v}}\right) \tag{4}$$

For the rotating region Eq. (5) was used to compute $\boldsymbol{T}$, where the splitting of Eq. (1) was utilized. The contribution of $\boldsymbol{v}^s \otimes \boldsymbol{v}^s$ is constant in time and space and consequently was neglected.

$$\boldsymbol{T} = b_s b_I \rho_0 \left(\boldsymbol{v}^r \otimes \boldsymbol{v}^r + \boldsymbol{v}^r \otimes \boldsymbol{v}^s + \boldsymbol{v}^s \otimes \boldsymbol{v}^r\right) \tag{5}$$

For the evaluation of these sources two spatial derivatives were consecutively applied to $\boldsymbol{T}$. For this purpose, a Gauss scheme was used because of its conservativeness. The sources were computed

for the rotating and the stationary domain separately and consequently no spatial derivative were computed across the interface. In order to avoid spurious noise arising due to this procedure, the damping function b_I was introduced, which was zero in two cell layers adjacent to the interface to set $\boldsymbol{T} = 0$. Another damping function b_s was used to damp sources of coarse cells far from the major source regions.

As an alternative to Lighthill's analogy, the acoustic perturbation equations (APE) were used. In their formulation APE-2 proposed by Ewert and Schröder [4], these are especially suited to incompressible flows. Furthermore, they provide a separation of p^a and p^h even in the source region. The original APE-2 requires for the solution of the scalar pressure and also the velocity, which sums up to four unknown scalar fields, that are expensive to be computed. The effort for this aeroacoustic approach was reduced by Hüppe and Kaltenbacher [5, 6] by deriving the perturbed convective wave equation (PCWE), which requires to solve only for the acoustic potential ψ by use of the non-homogeneous wave Eq. (6).

$$\begin{aligned} \frac{1}{c_0^2}\frac{\mathrm{D}\psi}{\mathrm{D}t} - \frac{\partial^2\psi}{\partial x^2} &= -\frac{b_s}{c_0^2}\frac{\mathrm{D}p^h}{\mathrm{D}t} \\ &= -\frac{b_s}{c_0^2}\Big(\underbrace{\frac{\partial p^h}{\partial t}}_{\mathrm{I}} \underbrace{+\boldsymbol{v}_c\frac{\partial p^h}{\partial x}}_{\mathrm{II}}\Big) \end{aligned} \tag{6}$$

After obtaining the solution of ψ, the acoustic pressure was calculated by Eq. (7) in a post-processing step, whereby the sound particle velocity could be computed by $\boldsymbol{v}^a = -\partial\psi/\partial x$. For the PCWE $\boldsymbol{v}_c = \overline{\boldsymbol{v}}$ was used in the stationary domain and $\boldsymbol{v}_c = \overline{\boldsymbol{v}^r}$ in the rotating domain, respectively.

$$p^a = \rho\frac{\mathrm{D}\psi}{\mathrm{D}t} \tag{7}$$

SIMULATION SETUP

The simulation domain for the acoustic propagation is depicted in figure 1. It features a settling chamber on the left where the air arrived. Subsequently, the air passed a small nozzle and arrived in the suction chamber above the radial housing. After flowing through the rotating impeller blades and a diffuser, the air was freely blown out. For the acoustic simulation the size of the box downstream to the diffuser was chosen to embed all microphones **mf1** to **mf5**, which were also used in the experiment. In contrast, this box was chosen larger for the flow simulation to inhibit any influence of the pressure outlet boundary condition on the jet downstream to the diffuser.

The flow simulations were performed by use of the commercial finite volume solver Star-CCM+. For the meshing the Trimmed meshing algorithm [7] was chosen, that creates meshes predominantly made of hexahedral cells. A section through the two used CFD meshes 1 and 2 is depicted in figure 2. The smallest cell size was chosen 0.6 mm for the coarse CFD mesh 1 and 0.38 mm for the finer CFD mesh 2 near the impeller blades and the tongue. The number of prism cell layers was set to four, which was not sufficient to yield a $y^+ \leq 1$, hence a wall model was used. In this figure, the rotating mesh region is coloured in red. This region was not chosen to be a cylinder, but a cylinder subtracted by a cylinder of smaller radius and featured only the blades of the impeller. The other rotating boundaries of the impeller were rotationally symmetric and modelled by a tangential wall velocity boundary condition during the simulation. This approach was found to be more efficient than using a full cylinder as rotating domain regarding the computation time. For the acoustic simulation the same splitting of

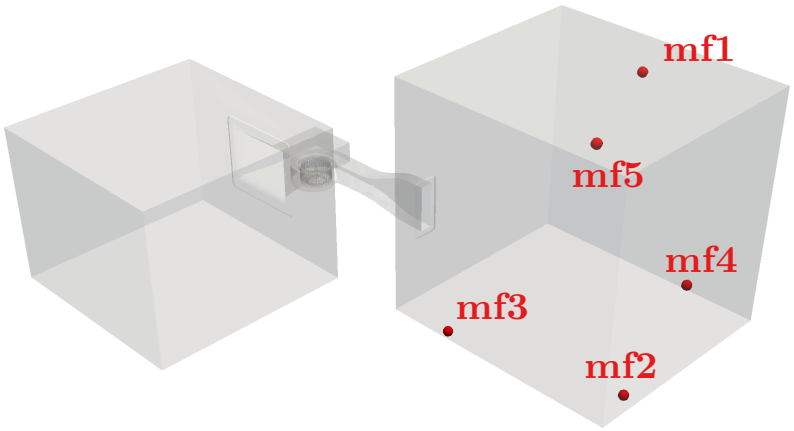

Figure 1: propagation domain of the acoustic simulation

rotating and stationary regions was performed. CFD mesh 1 consisted of about 10 mio. cells and CFD mesh 2 of about 26 mio. cells, respectively.

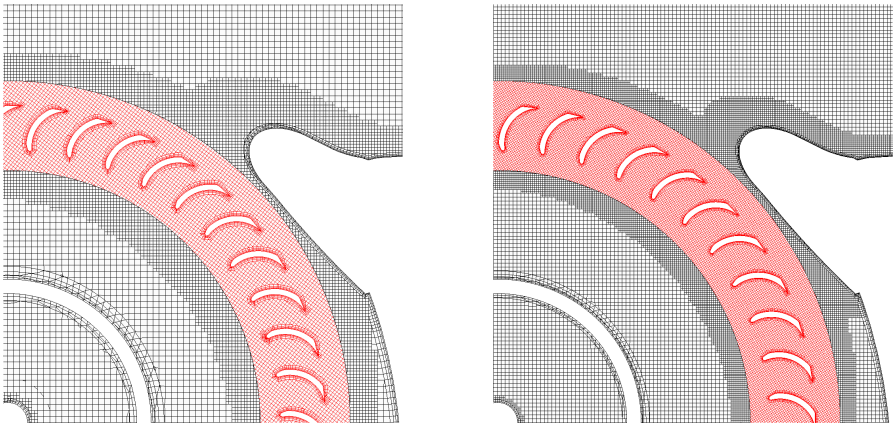

Figure 2: CFD mesh 1 (left) and CFD mesh 2 (right) near the tongue, rotating mesh is marked in red

A volume flow rate of 3.5 m^3/min was utilized as inlet boundary condition and zero pressure boundary condition at the outlet. A rotation rate of 1860 rpm was applied and a large eddy simulation (LES) was set up with use of the WALE subgrid scale model [8]. The time step size was chosen 10^{-5} s to yield CFL numbers of about 1 for both meshes. For the temporal discretization an implicit second order scheme was used and the SIMPLE solver algorithm was set-up. For the convective terms a bounded central difference scheme was chosen, whereas the gradient computation was done by a Green-Gauss scheme with MinMod Limiter. This set-up is much less dissipative than the default set-up of the solver [7], while still being stable for the given case. A steady RANS simulation was run to obtain initial flow fields for the LES, subsequently the LES simulation was run for about 20 revolutions and finally about 14000 time steps (0.14 s real time) were exported for the acoustic simulations, which includes more than four complete impeller revolutions. The pressure at the inlet was -169 Pa in the experiments, for CFD mesh 1 it was -177.95 Pa (5.3 % deviation) and for CFD mesh 2 it was -181.47 Pa (7.4 % deviation), hence the pressure jump of the fan was correctly predicted.

For the aeroacoustic simulations also two meshes were tested. In the suction chamber as well as in the far-field regions structured grids were created containing hexahedrons with an edge length of 14 mm for the CAA meshes. Inside the radial housing and at the impeller unstructured tetrahedron meshes were used. The unstructured and structured mesh parts were spliced by use of pyramid elements. The grid sizes of both meshed were varied at the impeller and the interfaces between rotating and stationary regions. While for the coarse CAA mesh 1 a size of 1.5 to 6 mm was chosen, it was set to 0.8 to 2 mm

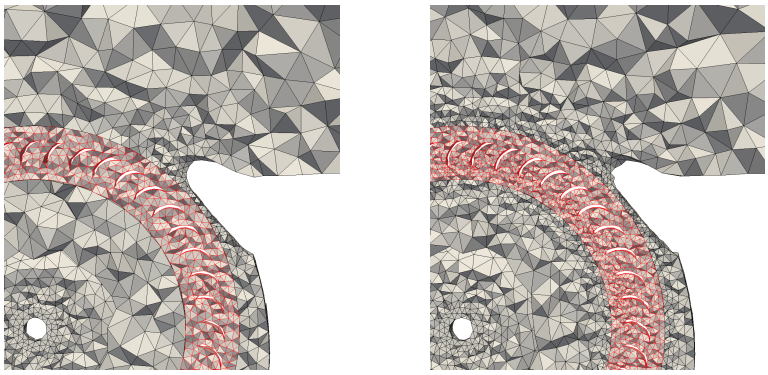

Figure 3: CAA mesh 1 (left) and CAA mesh 2 (right) near the tongue, rotating mesh is marked in red

for the fine mesh 2. An impression of these grids is given in figure 3. The radiation of sound waves across the interface was realized by use of the Nitsche's method[9]. At the boundary of the suction chamber and also in the far-field three element layers of perfectly matched layer (PML) [10] cells were added in order to suppress reflections and consequently to obtain a free sound radiation. The Hilber-Hughes-Taylor time integration method with $\alpha = -0.3$ was applied to yield a stable simulation [11]. For the source computation two spatial damping functions b_s were defined as shown in figure 4: one which contains sources of the jet and one which does not. The maximum Mach number inside the blade passages was about 0.09 and inside the jet about 0.023, hence it was lower by a factor of about four inside the jet, and consequently the sound radiated from the jet was expected to be masked by the sound of the impeller.

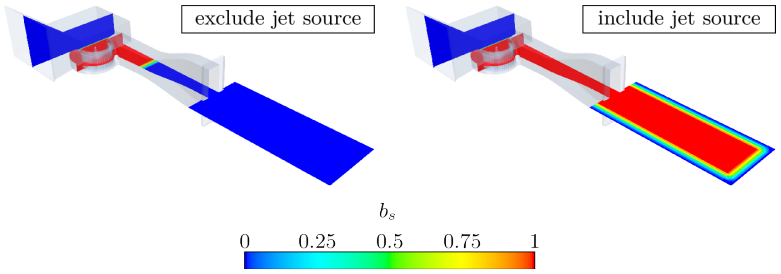

Figure 4: Spatial damping functions b_s

ACOUSTIC SOURCES AND PROPAGATION

The acoustic sources obtained from the flow field of CFD mesh 1 are depicted in figures 5 and 6. The sources of Lighthill and PCWE are of different units, thus they are not comparable regarding their amplitudes but only with respect to their spatial distribution. The highest source amplitudes appeared near to the impeller at the upstream and downstream edges of the blades. There seem to be also strong sources at both sides if the interface in case of Lighthill's analogy, that appeared due to the damping function b_I, which was introduced because the spatial derivatives were not evaluated across the interface. However, the quadrupole nature of Lighthill's sources was preserved by this procedure, by omitting the quadrupole contributions of two cell layers adjacent to each interface side. The sources of PCWE revealed a jump between stationary and rotating regions near to the tongue, which arose due to the different velocities $\overline{\boldsymbol{v}}$ and $\overline{\boldsymbol{v}^r}$ used during the evaluation of the right-hand side of Eq. 6 on both sided of the interface. This resulted in a red spot in the rotating domain near the tongue (see figure 5), which appeared due to term II in Eq. 6. This term is a product of the spatial derivative of the flow pressure with the mean velocity in rotating frame $\overline{\boldsymbol{v}^r}$, while the former remained almost constant due to

the high number of bladed, the latter was almost identical for each blade passage. Thus, the red spot remained approximately constant in space and time and consequently did not propagate significant noise contributions.

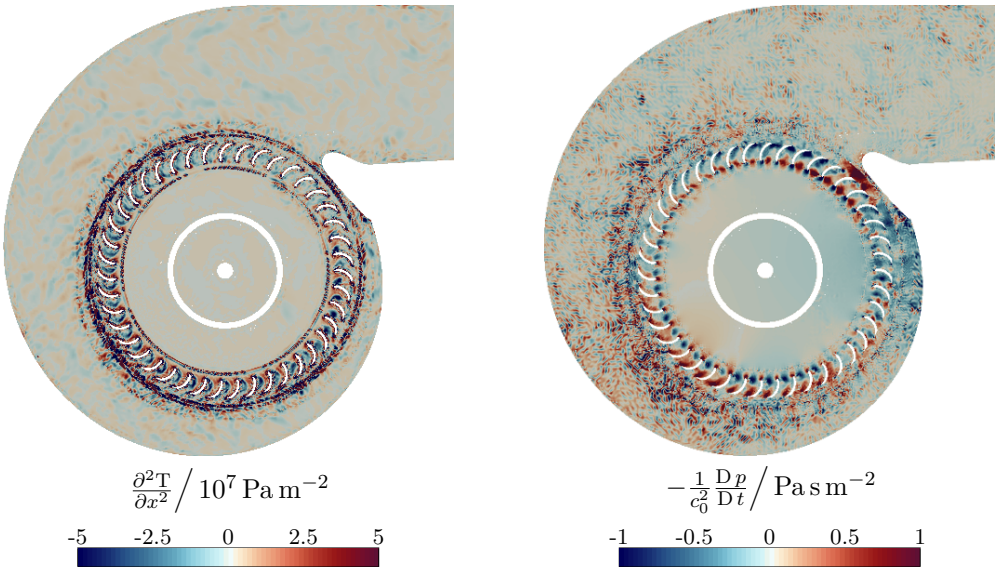

Figure 5: Acoustic sources at the impeller computed from CFD mesh 1 for Lighthill's analogy (left) and for PCWE (right) at one time step

In figure 6 sources in the jet region are shown, which were much smaller regarding their amplitudes in comparison to the sources close to the blades. The sources of Lighthill's analogy still look similar to flow structures of passing vortices. The sources of the PCWE did not reveal these structures and appeared noisy due to the required temporal derivative of the flow pressure. This derivative contains a lot of high frequency components, which was also revealed by the spectra presented in the following section. These noisy high frequency components dominate this source image.

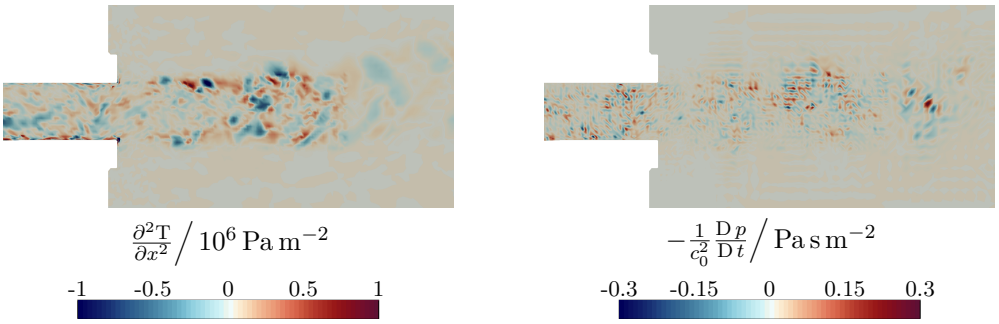

Figure 6: Acoustic sources in the jet region computed from CFD mesh 1 for Lighthill's analogy (left) and for PCWE (right) at one time step

After performing the CAA simulation acoustic fields were received, which are shown for one instantaneous time step in figure 7. The ranges for the pressure were chosen differently for Lighthill's analogy and the PCWE, because the field obtained from Lighthill's analogy still incorporated flow pressure fluctuations inside the source region, which were not present for PCWE. Moreover, a pressure jump occurred at the interface in case of Lighthill's analogy, which was caused by the subtraction of different mean Lighthill tensor fields in the stationary and rotating domains. In contrast, the acoustic field obtained from the PCWE is consistent across the interface.

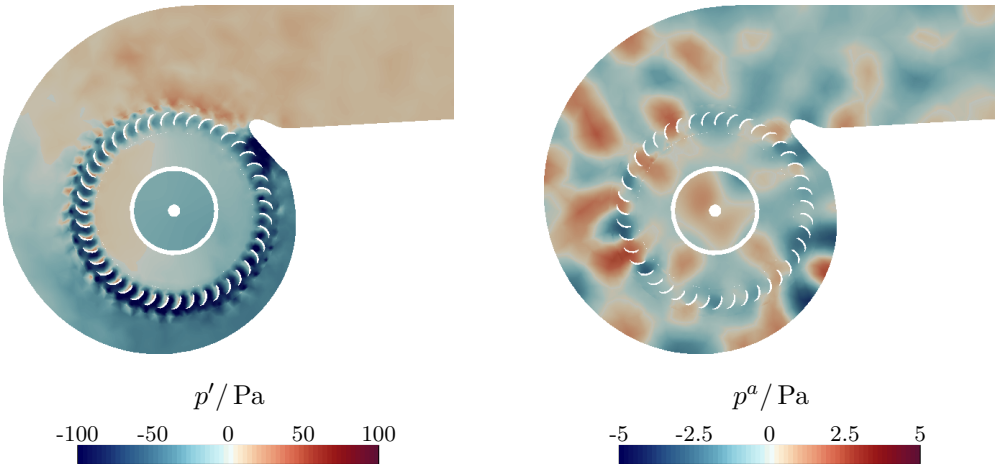

Figure 7: Result of acoustic propagation simulation at one time step at CAA mesh 1 with sources from CFD mesh 1 for Lighthill's analogy (left) and for PCWE (right)

INFLUENCE OF THE SIMULATION PARAMETERS ON SPECTRA

The influence of the acoustic sources in the jet region on the overall far-field noise is illustrated by means of the power spectral density (PSD) plotted in figure 8 against the frequency. This comparison reveals, that these jet sources are of minor influence on the acoustics far from the fan. This is not surprising, because the amplitudes of these sources were already much lower than that at the impeller, which confirms previously made assumption based on Mach number analysis. Due to the accordance of the results with such classical estimations, the used numerical methods were proven to work correctly. Lighthill's analogy and the PCWE behaved in the same way with respect to the inclusion of the jet sources. As a consequence, only the sources excluding the jet were used for the assessment of the other simulation parameters presented in the following.

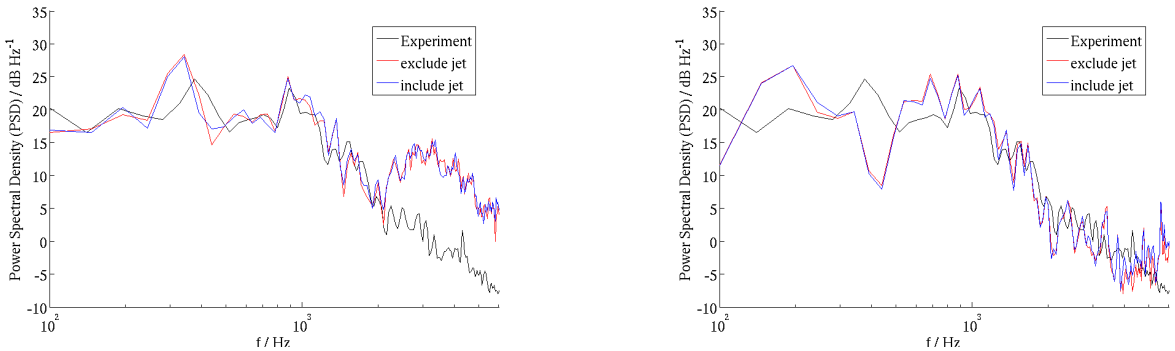

*Figure 8: PSD spectra at **mf5** obtained from CFD mesh 2 and CAA mesh 1 for Lighthill's analogy (left) and for PCWE (right) with use of different damping function*

The next subject of interest was the influence of the CAA mesh size on the far-field spectra. The given CAA meshes only vary in their cell size near the impeller, where the strongest sources were observed. PSD spectra obtained using these meshes are depicted in figure 9. In the case of PCWE, there was no major influence of the mesh size in the source region onto the far-field noise spectra. However, if Lighthill's analogy was used, the spectra obtained with CAA mesh 1 overestimated the sound pressure for frequencies larger than about 2000 Hz, whereas such an overestimation was observable at about 4000 Hz for CAA mesh 2. This effect was caused by the missing separation of flow and acoustic pressure fluctuations inside the source regions. The acoustic solver had to reproduce the pressure fluctuations of the flow solution, which can be only done if the acoustic mesh sufficiently resolves

the scales of these fluctuations. The same effect was previously shown for the simulation of a HVAC unit[12].

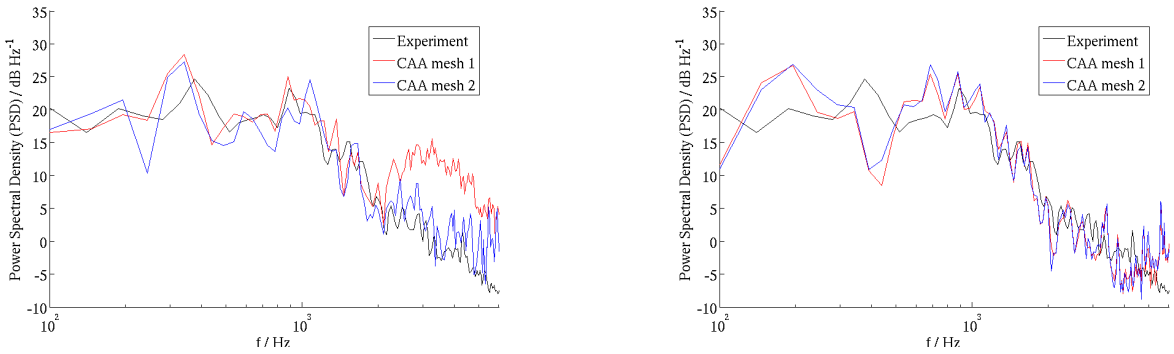

*Figure 9: PSD spectra at **mf5** obtained from CFD mesh 2 for Lighthill's analogy (left) and for PCWE (right) with use of different CAA meshes*

All previously shown spectra were obtained with use of flow results of CFD mesh 2. A comparison to those obtained from use of CFD mesh 1 are shown in figure 10. For the coarse mesh the spectrum of the PCWE is dominated by noise for frequencies larger than about 2000 Hz. If the CFD mesh size becomes too coarse, aliasing induces noise in the flow field at high frequencies. This effect yields spurious noise especially in the pressure signal and not so much in the velocity signal[12]. Therefore, the PCWE, of which the acoustic sources are computed from the flow pressure, is more sensitive with respect to CFD mesh coarsening than Lighthill's analogy regarding the numerical noise level.

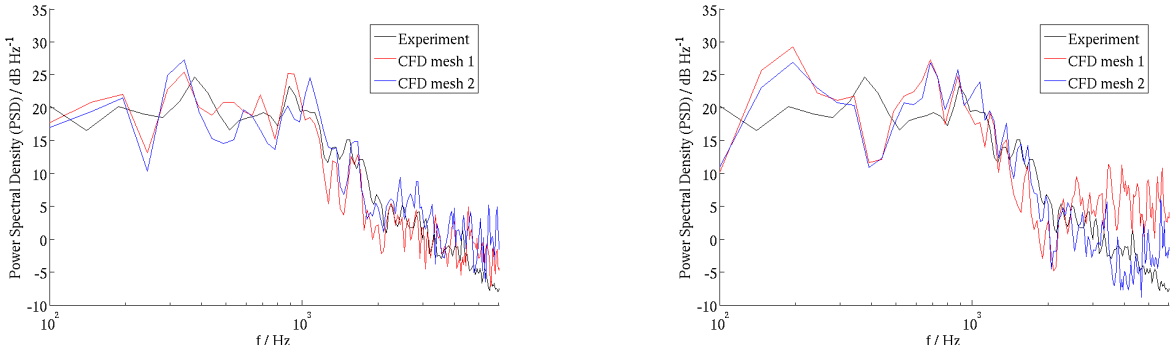

*Figure 10: PSD spectra at **mf5** obtained from CAA mesh 2 for Lighthill's analogy (left) and for PCWE (right) with use of different CFD meshes*

Finally, spectra are shown in figure 11 to compare Lighthill's aeroacoustic analogy to the PCWE, whereby the finest CFD and CAA meshes were utilized. Both approaches were able to predict the experimental results very good up to frequencies of about 5000 Hz. This was also the case for varying microphone positions, which reveals the good agreement of the acoustic propagation simulations with respect to the sound radiation directivity.

CONCLUSION

Lighthill's aeroacoustic analogy and the acoustic perturbation equations in form of the PCWE were both able to predict the far-field noise which was emitted by a radial blower. This was shown by comparison to PSD spectra from experimental results. The PCWE requires the flow pressure as main input variable, which is more sensitive to numerical noise than the velocity, that is used by Lighthill.

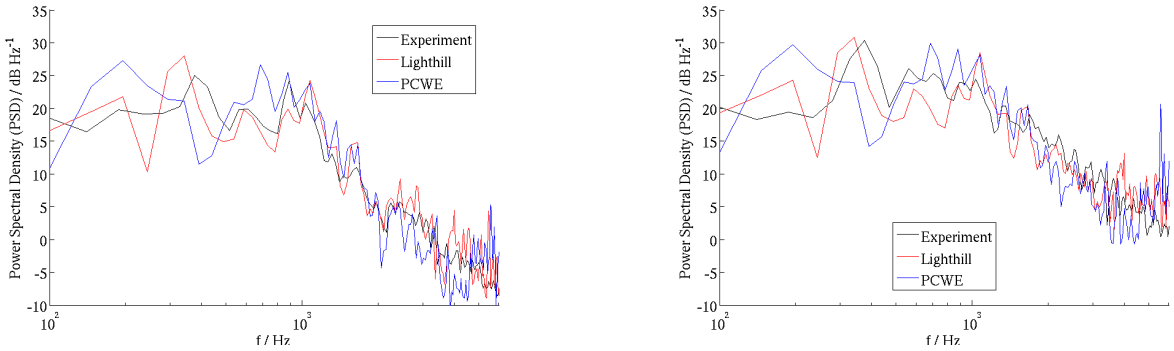

*Figure 11: Comparison of PSD spectra obtained from Lighthill's analogy and PCWE with CFD mesh 2 and CAA mesh 2 at microphone **mf1** (left) and **mf3** (rigtht)*

Major disadvantages of Lighthill's analogy are the missing separation of flow and acoustic pressure fluctuations and the high requirements for acoustic grid refinements in the source regions. Moreover, the sources of Lighthill's analogy may be hard to interpret, if the derivatives are not evaluated across the interface like done in this work.

REFERENCES

[1] M. Kaltenbacher. *Advanced simulation tool for the design of sensors and actuators*. Procedia Engineering, 5:597–600, **2010**.

[2] M. J. Lighthill. *On sound generated aerodynamically. I. General theory*. In *Philos. Trans. Royal Soc. London. Series A*, volume 211, pages 564–587. The Royal Society, **1952**.

[3] M. J. Lighthill. *On sound generated aerodynamically. II. Turbulence as a source of sound*. In *Philos. Trans. Royal Soc. London. Series A*, volume 222, pages 1–32. The Royal Society, **1954**.

[4] R. Ewert and W. Schröder. *Acoustic perturbation equations based on flow decomposition via source filtering*. J. Comput. Phys., 188(2):365–398, jul **2003**.

[5] A. Hüppe, J. Grabinger, M. Kaltenbacher, A. Reppenhagen, G. Dutzler, and W. Kühnel. *A Non-Conforming Finite Element Method for Computational Aeroacoustics in Rotating Systems*. In *20th AIAA/CEAS Aeroacoustics Conference*. American Institute of Aeronautics and Astronautics, jun **2014**.

[6] M. Kaltenbacher, A. Hüppe, A. Reppenhagen, M. Tautz, S. Becker, and W. Kuehnel. *Computational Aeroacoustics for HVAC Systems Utilizing a Hybrid Approach*. SAE International Journal of Passenger Cars - Mechanical Systems, 9(3), jun **2016**.

[7] *Star-CCM+ 11.06.010 User Guide*. Siemens Product Lifecycle Management Software Inc., **2017**.

[8] F. Nicoud and F. Ducros. *Subgrid-scale stress modelling based on the square of the velocity gradient tensor*. Flow, Turb. Comb., 62(3):183–200, **1999**.

[9] J. Nitsche. *Über ein Variationsprinzip zur Lösung von Dirichlet-Problemen bei Verwendung von Teilräumen, die keinen Randbedingungen unterworfen sind*. Abhandlungen aus dem Mathematischen Seminar der Universität Hamburg, 36(1):9–15, jul **1971**.

[10] B. Kaltenbacher, M. Kaltenbacher, and I. Sim. *A modified and stable version of a perfectly matched layer technique for the 3-d second order wave equation in time domain with an application to aeroacoustics*. J. Comput. Phys., 235:407–422, **2013**.

[11] H. M. Hilber, T. J. R. Hughes, and R. L. Taylor. *Improved numerical dissipation for time integration algorithms in structural dynamics*. Earthquake Engineering & Structural Dynamics, 5(3):283–292, jul **1977**.

[12] M. Tautz, A. Hüppe, K. Besserer, M. Kaltenbacher, and S. Becker. *Aeroacoustic Simulation of Complex HVAC Components*. In *ICTCA 2017 Vienna - Book of Abstracts*, **2017**.

ACKNOWLEDGEMENTS

This research work was partially supported by COMET—Competence Centers for Excellent Technologies Program of the Austrian Federal Ministry for Transport, Innovation and Technology, the Austrian Federal Ministry of Science, Research and Economy, the Austrian Research Promotion Agency, the Province of Styria, and the Styrian Business Promotion Agency.